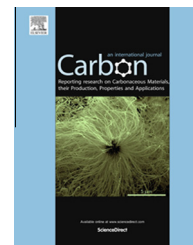


Available at www.sciencedirect.com

ScienceDirect

journal homepage: www.elsevier.com/locate/carbon

Tunable, self-assembled 3D reduced graphene oxide structures fabricated via boiling

HangJin Jo ^a, Hyunwoo Noh ^b, Massoud Kaviany ^{a,c}, Ji Min Kim ^b, Moo Hwan Kim ^a,
Ho Seon Ahn ^{d,*}

^a Division of Advanced Nuclear Engineering, POSTECH, Pohang 790-784, Republic of Korea

^b Department of Mechanical Engineering, POSTECH, Pohang 790-784, Republic of Korea

^c Department of Mechanical Engineering, University of Michigan, Ann Arbor, MI 48109, USA

^d Division of Mechanical System Engineering, Incheon National University, 406-722, Republic of Korea

ARTICLE INFO

Article history:

Received 12 June 2014

Accepted 18 September 2014

Available online 28 September 2014

ABSTRACT

To exploit the favorable mechanical and electrical properties of graphene in practical applications, control over the dimensionality and geometry of assembled graphene structures is required. Here, we report the use of boiling with reduced graphene oxide (RGO) colloidal dispersion to form self-assembled three-dimensional (3D) RGO structures. The morphology of the resulting self-assembled RGO structures could be controlled by varying the heat flux during boiling. A large heat flux resulted in continuous bubble nucleation at the surface, and consequently, the interference exhibited aggregates of RGO flakes around the bubble nucleation site due to repetitive expansion and contraction of the bubble triple line. As the water evaporated, self-assembled foam-like graphene (SFG) was formed. As the heat flux increased, more vigorous agitation occurred at the interface, which led to smaller pores in the structures. With a low heat flux, the less vigorous bubble interference dynamics led to interactions between the RGO flakes, and consequently, self-assembled bump-like graphene (SBG) structures were formed, which were not porous. The self-assembled RGO 3D structures exhibited favorable mechanical and electrical properties compared with conventional 3D self-assembled graphene- or carbon-based structures. Such controllable 3D RGO structures with good mechanical and electrical properties have potential applications.

© 2014 Elsevier Ltd. All rights reserved.

1. Introduction

Graphene is a two-dimensional monolayer of carbon, and has received much recent research attention because of its favorable mechanical, electrical, and thermal properties [1–10]. The initial study of the graphene focused on methods to realize high-quality two-dimensional graphene monolayers to exploit these properties. However, to utilize graphene in applications including energy storage and conversion [11],

electrocatalysis [12,13], supercapacitors [14,15], conducting membranes [16–21], and biochemical sensors [22–24], control over the dimensionality and geometry of graphene is desirable.

Several methods to synthesize integrated structures formed of graphene sheets have recently been developed [25]. The ‘breath-figure’ method [26–28] employs polymer-grafted graphene oxide (GO) platelets and condensation at the solution surface under moist conditions to form porous

* Corresponding author.

E-mail address: hsahn@incheon.ac.kr (H.S. Ahn).

<http://dx.doi.org/10.1016/j.carbon.2014.09.068>

0008-6223/© 2014 Elsevier Ltd. All rights reserved.

reduced graphene oxide (RGO). The morphology of the open porous structures is determined by the concentration of the organic precursor dispersion and the length of the polymer chains grafted onto the GO flakes. Using micron-sized particles as a template with stable aqueous dispersions of graphene in the presence of a polymer can form three-dimensional (3D) graphene–polymer nano-composite structures [29,30]. Nano-structured graphene-based systems have been fabricated by inducing bonding of an aqueous dispersion of graphene sheets with a copolymer [31] and novel metal nanoparticles [32] using centrifugal evaporation [33] and reduction procedures [34–36]. Recently, Chen et al. [37] synthesized high-quality 3D graphene macroscopic structures with a foam-like network of graphene using template-directed chemical vapor deposition. The graphene sheets in the foam were interconnected to form a flexible 3D network with a large electrical conductivity. However, these techniques require a high level of control over the environment conditions and involve long reaction times. To address this, recent researchers used graphene gelation [38] or used a dilute aqueous suspension of pristine graphene [39].

Ahn et al. [40,41] produced also 3D self-assembled foam-like graphene (SFG) using nucleate boiling in RGO colloidal water dispersion, which is a low-cost and low-temperature process that is suitable for large-scale synthesis and not dependent on a particular substrate. However, the synthesis of 3D graphene structures using boiling in RGO colloidal water dispersion requires further work. In particular, the details of the mechanism of formation of RGO 3D structures during boiling are not fully understood. Here, we report two different self-assembled graphene structures formed by boiling RGO colloidal dispersions. The structural properties are dependent on the heat flux. We describe the mechanism of self-assembly during nucleate boiling by considering the bubble dynamics and the effect on the RGO flakes around the bubble. We characterize the mechanical and electrical properties of the resulting self-assembled RGO 3D structures.

2. Experimental facility and procedure

2.1. RGO colloidal dispersion preparation

The RGO colloidal dispersion was prepared from graphite powder by oxidation and subsequent reduction. First, the graphite was oxidized to form GO using the modified Hummers method [42,43]. 2 g of graphite (<45 mm, Aldrich) and 1 g of sodium nitrate (Aldrich) were dispersed in 50 ml of sulfuric acid (ACS 95–98%, Alfa Aesar) at a temperature below 10 °C. Vigorous stirring was applied during the entire synthesis process. 6 g of potassium permanganate (Aldrich) was slowly added over a period of 30 min. The solution was then heated to 35 °C for an additional 2 h. 100 ml of deionized (DI) water was then dropped onto the solution very slowly over 10 min, and the solution was allowed to react at less than 95 °C for a further 30 min, resulting in a brown solution of graphite oxide (GO). To neutralize the metallic salt and residual acid, 40 ml of hydrogen peroxide solution (36 ml of DI water and 4 ml of hydrogen peroxide solution (30 wt%, Aldrich)) was added, and membrane filtration was carried

out twice. The resulting GO was freeze-dried to form GO powder.

The GO was reduced to form RGO colloids using hydrazine [44]. 500 ml of a 0.5-mg/ml GO colloidal dispersion in DI water was prepared by exfoliation using ultrasonication (Fisher Scientific Sonic Dismembrator, Model 500, 400 W, 20 kHz, 30% amplitude) for 1 h. The colloidal dispersion was heated to 95 °C, and then 3.5 ml of ammonia solution (28–30 wt%, Samchun) and 0.5 ml of hydrazine solution (35 wt%, Aldrich) were added, and allowed to react for 1 h. The colloidal dispersion turned from a transparent brown to an opaque black, which is indicative of the formation of RGO (see Fig. S1 in the Supplemental materials).

2.2. Boiling experimental facility and procedure

To investigate the details of the formation mechanism of the self-assembled RGO structures, we designed a single-bubble experiment using a platinum thin film as the heating element (Fig. 1). Single-bubble pool-boiling experiments were conducted under saturated atmospheric conditions with deionized (DI) water as the working fluid. The facility was composed of a sample jig, a main test pool, an immersion heater and a condenser. The sample jig was made by polyetheretherketone (PEEK) which has low thermal conductivity, and good mechanical, chemical and electrical resistance. A silicon wafer specimen was fixed on the sample jig. The main test pool was a rectangular aluminum bath. A proportional–integral–derivative (PID) controller was used with the immersion heater and the reflux condenser was installed to maintain the saturated conditions. A high-speed camera (Integrated Design Tools, Inc., Y7) was installed on the window to visualize bubble dynamics.

A 150-nm-thick platinum layer was deposited on one side of the wafer for the heater, and boiling was induced on the other side of the wafer. The silicon specimen had a SiO₂ layer (5000 Å) on both sides for electrical insulation, and the size of the specimens was 25 × 20 mm. The electrodes were connected to a power supply to allow Joule heating. Single bubbles were generated from the heater which was circular with a diameter of 1 mm. Single bubbles were generated for 10 min with a constant heat flux. All experiments were carried out following a 2-h degassing procedure. With the system open to ambient air pressure via the reflux condenser, the dissolved air was expelled while the steam was condensed and returned to the vessel. The heat flux and wall temperature were evaluated from the measured voltage and current through the wires. In particular, the wall temperature was determined from the measured resistance of the heater and an empirically derived correlation between the resistance and wall temperature. Atomic force microscopy (AFM, Veeco Dimension 3100 + Nanoscope V) was used to determine the roughness of the surfaces, which were $R_a = 4.9$ nm, $R_q = 6.6$ nm, and $R_{max} = 50.8$ nm.

3. Results and discussion

Self-assembled RGO 3D structures were formed using boiling with 0.005 g/L RGO colloidal dispersions, as shown in Fig. 2. The morphological characteristics of the self-assembled

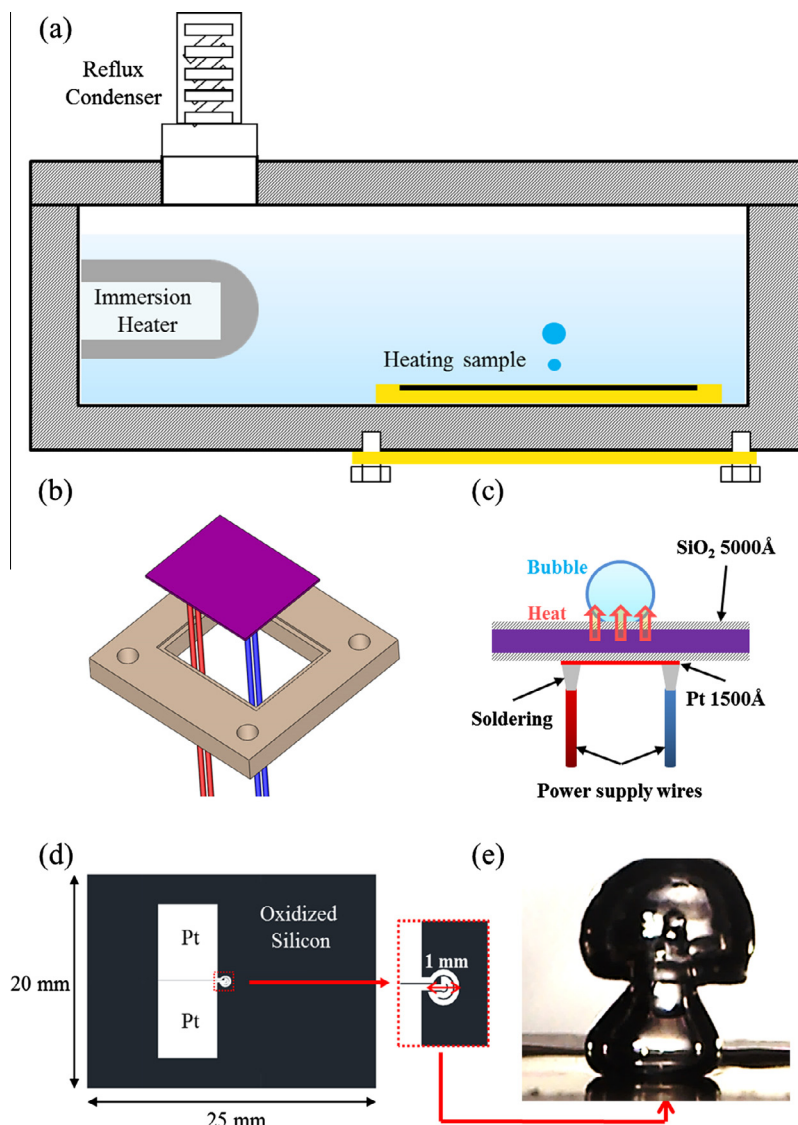


Fig. 1 – (a) Experimental facility used to generate single bubbles under saturated atmospheric conditions. (b) The heated surfaces used in experiments from (c) the side view and (d) the bottom view, and (e) an image showing the bubble dynamics on the heated surface. (A color version of this figure can be viewed online.)

graphene structures that formed on the heated surface depended on the supplied heat flux. At $q'' = 11,000 \text{ kW/m}^2$ (*heat flux A*), the self-assembled bump-like graphene (SBG) structures formed at the heated surface, as shown in Figs. 2b and 3a. The length scales of bump structures formed at *heat flux A* are the order of a few to tens of microns. Basically the bump structures were sparsely spread out on the heating area, but some of them were linked together by RGO flake layer. However, when a heat flux of $q'' = 15,000 \text{ kW/m}^2$ (*heat flux B*) was applied with the same concentration of RGO colloids, porous SFG structures were formed, as shown in Figs. 2d and 3b. SFG structures consist of complicatedly linked RGO bridges and micron pores. The resulting RGO structures had features with a micrometer scale, which is significantly smaller than the diameter of the departing bubbles ($\sim 5 \text{ mm}$). Therefore, the formation of micron-sized islands or pores may not be directly related to the behavior of the departing bubbles. Furthermore, the

self-assembled RGO structures were only formed on the heating area (circular with a diameter of 1 mm), even if the triple line of the nucleated bubble maximally expanded more than 3 times of the heating area (see Fig. S2 in the Supplemental materials). It allows inferring that the formation of the self-assembled RGO structures is not directly related with the bubble expansion dynamics.

To investigate the similarity of the formation procedure of bumps and porous structures during the initial stages of formation, we reduced the boiling time to 1 and 5 min for the same heat fluxes (Fig. 3c and d). Even though the total number of bubbles generated was reduced by the shorter duration of boiling, the surface heated with *heat flux B* exhibited porous structures without bumps. This suggests that the morphological characteristics of the self-assembled graphene originate from the intrinsic behavior with respective heat flux, and are not dependent on the boiling time or deposition time.

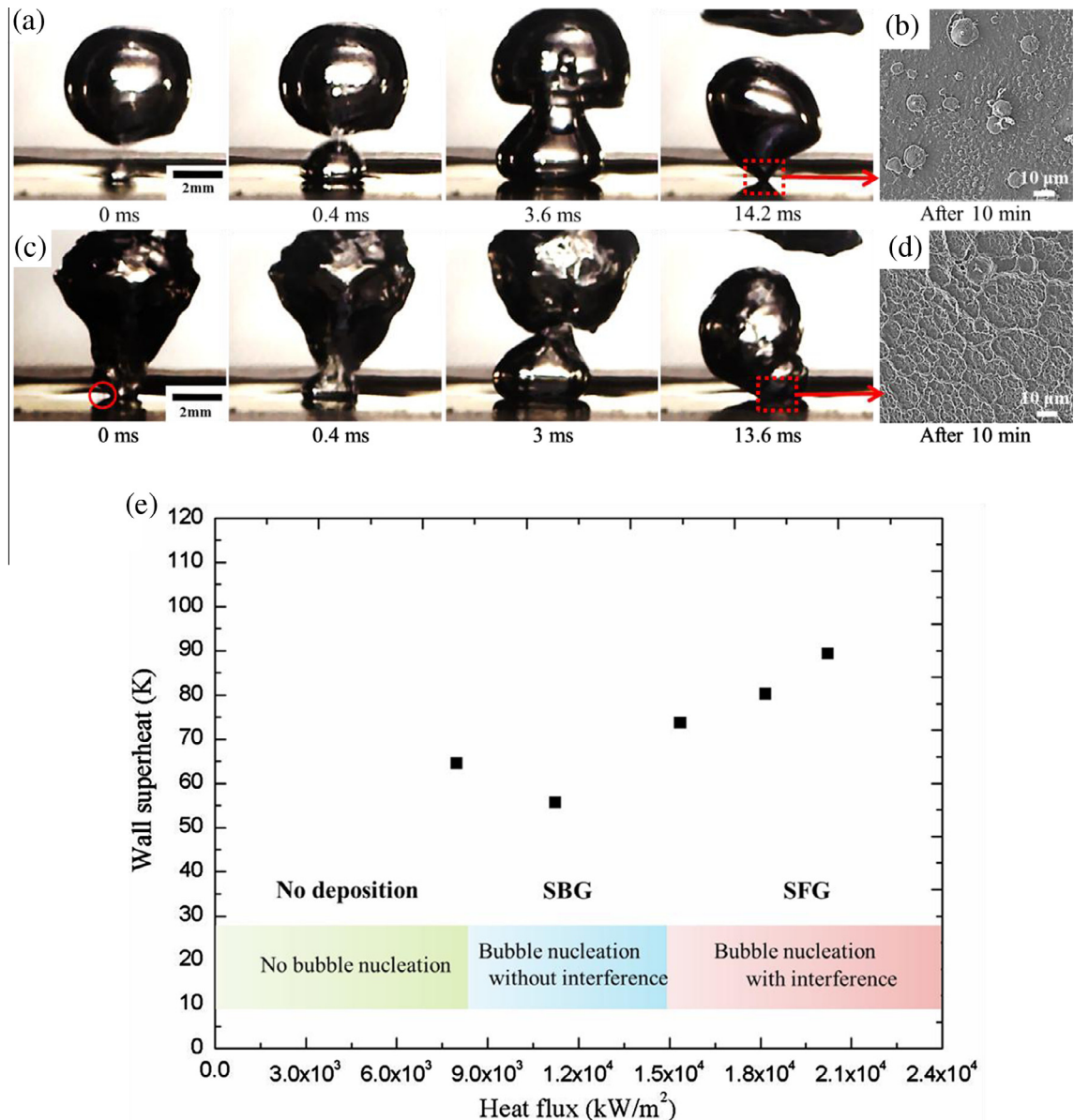


Fig. 2 – (a) Bubble dynamics and (b) scanning electron microscopy (SEM) image of the heated surface following boiling with the RGO colloidal dispersion for 10 min using a heat flux of 11,000 kW/m². (c) Bubble dynamics and (d) SEM image of the heated surface following boiling with the RGO colloidal dispersion for 10 min using a heat flux of 15,000 kW/m². (e) Boiling curves of the RGO colloidal dispersions under saturated atmospheric conditions. (A color version of this figure can be viewed online.)

According to scanning electron microscopy (SEM, LEO SUPRA35) images and transmission electron microscopy (TEM, JOEL JEM-2200FS with an image Cs-corrector) images, SFG initially had well-aligned RGO sheets with sub-micron thickness (Fig. 4). It is expected that the van der Waals' forces between the heated surface and the RGO flakes were dominant, leading to well-aligned deposition. Farther from the heated surface, the effect of van der Waals' forces between the surface and the RGO flakes were weaker. Consequently, the interactions between the RGO flakes suspended in the water were dominant in the formation of self-assembled structures. During this process, the heat flux determines the liquid flow around the nucleating bubble, providing opportu-

nities to form bonds between RGO flakes located at or near the bubble interface. Therefore, by analyzing the dynamics of the bubbles and the RGO suspended colloids, we should be able to describe the formation of bumps or porous structures at different heat fluxes.

The principal difference between the SBG structures formed with *heat flux A* and the SFG structures formed with *heat flux B* was the presence of the bubble interference. The corresponding surface superheats with each heat flux were also different: ~50 K and 70 K, respectively (Fig. 2). However, it is not clear that a difference of 20 K will lead to significantly different formation processes, resulting in bumps or porous structures. With *heat flux B*, the measured departing diameter

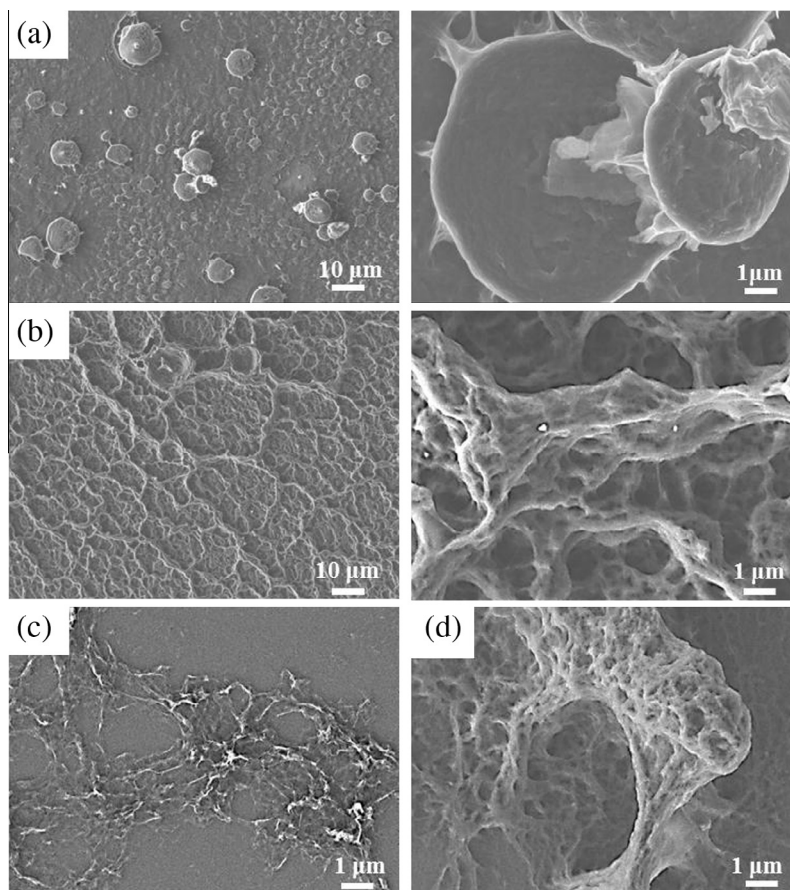


Fig. 3 – SEM images showing the surface morphology following boiling for (a) 10 min at $q'' = 11,000 \text{ kW/m}^2$, (b) 10 min at $q'' = 15,000 \text{ kW/m}^2$, (c) 1 min at $q'' = 15,000 \text{ kW/m}^2$, and (d) 5 min at $q'' = 15,000 \text{ kW/m}^2$.

of the bubbles was 5.3 mm and the maximum expanded base diameter was 3.6 mm, which is similar to the values obtained with *heat flux A*, where the departure diameter was 4.8 mm and the equilibrium base diameter was 3.3 mm. The frequency of bubble generation was 64 Hz with *heat flux B* and 58 Hz with *heat flux A*. The expansion velocity of the interface was 2.6 m/s with *heat flux A* and 3.6 m/s with *heat flux B*. The velocity difference of induced flow velocity by bubble was just 1 m/s. Therefore we supposed that the effect of different velocity on producing self-assembled RGO structure was negligible. The main distinction was that *heat flux B* exhibited continuous bubble nucleation with no time gaps between departing bubbles (Fig. 2c). During bubble departure, the following bubble nucleates from the center of the heated surface. With *heat flux A*, a period of time was required for the next bubble to form, whereas with *heat flux B*, a wetted area at the bubble nucleation site existed for only a very short time.

It appears that the frequent bubble generation and the interference between successive bubbles were related to the nature of the formation of the RGO structures at the surface, as shown in Fig. 5. During frequent bubble nucleation at the heated surface, bubbles, which do not include dispersed RGO flakes, generate a liquid counter phase in which the dispersed RGO flakes are more concentrated. The bubble expansion in boiling is accompanied by mass change from liquid to

water. It means that as boiled bubble expands the amount of liquid decreases, therefore the local concentration of RGO spontaneously increase. In particular, near phase interface the concentration change of RGO would be significant. At the interference between bubbles during repetitive expansion and contraction of the triple line, the concentrated RGO regions tend to aggregate during boiling. As the triple line shrinks during bubble departure, RGO sheets near the interface are dragged toward the center of the heated surface because of amphiphilic properties of RGO [45]. The RGO sheets are pushed away again by the following bubble nucleation, as shown in Fig. 5a. During this motion, the RGO sheets are able to make contact with each other, and induce π - π interactions between π -conjugated bonds, leading to stacking of the RGO sheets. However, this bonding may not be consolidated due to perturbations from the unsteady flow. It follows that only parts of the RGO sheets can become connected with other RGO sheets; other parts of the RGO sheets are linked with water molecules via the oxygen functional group on the RGO sheets.

We used atomic force microscopy (AFM) to characterize the thickness of the RGO flakes, which was $\sim 0.7 \text{ nm}$, exceeding that of a single graphene layer (0.334 nm) (see Fig. S3 in the Supplemental materials) [40]. The difference in thickness was attributed to the interaction between Si wafer and RGO, and existence of oxygen functional groups on the RGO flakes.

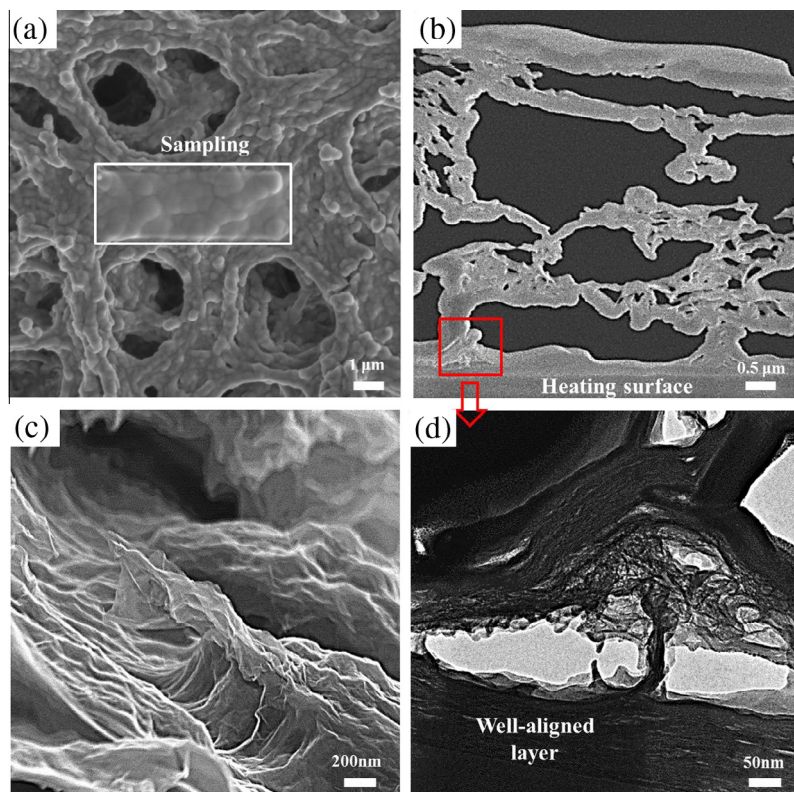


Fig. 4 – SEM images of 3D self-assembled foam-like graphene (SFG) from (a) the top view and (b) the side view. (c) SEM image of the well-aligned layer formed adjacent the heated surface and (d) TEM image showing the pores and well-aligned structures. (A color version of this figure can be viewed online.)

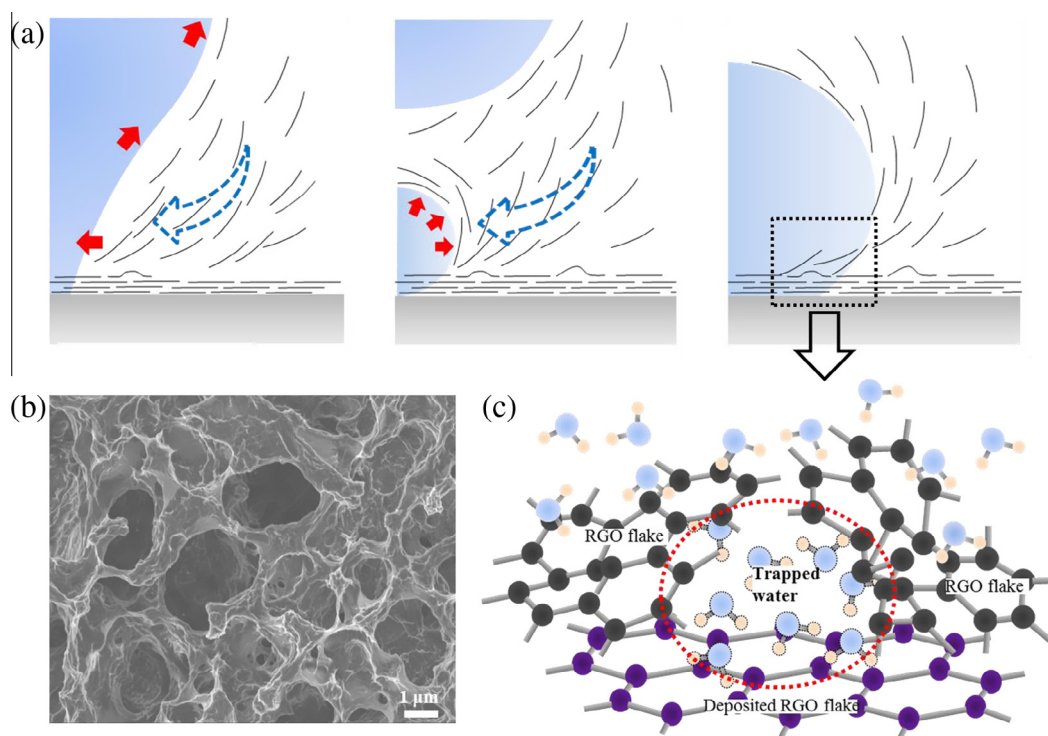


Fig. 5 – (a) Schematic diagram of the RGO flakes during interference between departing and nucleating bubbles. (b) SEM image of the pore structures formed by RGO flakes during bubble interference and (c) schematic diagram of the formation mechanism of the SFG pore structures. (A color version of this figure can be viewed online.)

Since RGO was reduced from GO, some oxygen functional groups were expected to remain. X-ray photoemission spectroscopy (XPS) data showed that the RGO sheets had the peaks corresponding to oxygen functional groups (see Fig. S4 in the Supplemental materials). The oxygen functional groups is hydrophilic; therefore, the π - π stacking between RGO sheets is influenced by the existence of water, which is attracted to the oxygen functional groups on the RGO flakes [35,46]. Water molecules would attract each other due to hydrogen bonding between water molecules. Therefore the bound water by the oxygen functional group on RGO flakes allow to the presence of water cluster near the RGO flakes. According to AFM result, the size of RGO flake in the lateral direction is 1–3 μm (see Fig. S3 in the Supplemental materials). If RGO flakes linked together, the space of water between RGO flakes would be a few to tens of microns. It follows that as the water evaporates, the space occupied by the water becomes a pore in the structure formed by the interconnected RGO flakes.

To reproduce the formation mechanism of RGO porous structures, we heated a 0.3-g/L RGO colloidal dispersion in a Teflon-lined autoclave at 150 °C for 10 h. The hydrothermal synthesis of RGO in the autoclave was conducted to classify the pore and island formation mechanisms. Conceptually, it is supposed that the van der Waal's forces between the heated surface and the RGO flakes were dominant, leading to well-aligned deposition near the heated surface. Farther from the heated surface, the effect of a solid substrate was weaker. Consequently, the interactions between the RGO flakes suspended in the water were dominant in the formation of self-assembled structures. Particularly, important parameters are the RGO contact opportunities and water evaporation within RGO flakes. It is supposed that autoclave experiment is well describing these parameters, although the experiment could not include the effect of a solid substrate on the formation of RGO structures. Because there was no phase change in

the Teflon-lined autoclave, we intentionally raised the concentration of RGO colloids from the 0.005 g/L that was used in the boiling experiments. Furthermore, the time in the autoclave was increased to compensate for the high contacting opportunity between the RGO flakes during bubble interferences.

As a result, the RGO sheets formed aggregates and precipitation was observed, as shown in Fig. 6a. The volume of the precipitates aggregated in the high-concentration colloids immediately following removal from the bulk solution was larger than the volume of the aggregations following drying, as shown in Fig. 6b. It follows that water occupied a certain volume in the interconnected RGO sheets. Because of the water evaporation, the total volume of precipitates decreased following drying. The shrunken precipitates had densely compact structures without pores, as shown in Fig. 6c and d. We assumed that the space occupied by water in the RGO sheets collapsed during the slow evaporation. To induce faster evaporation, we removed the precipitates from the bulk colloids, and then substituted the working fluid from a water-based to an ethanol-based colloidal dispersion. However, porous structures were not observed. We then supplied heat to accelerate the evaporation, which resulted in the formation of porous structures, as shown in Fig. 6e and f. Because the aggregations of RGO sheets were produced before changing the solvent, the different wetting properties of the two solvents would affect the size of spaces occupied by water or ethanol, and it could influence the formed pore size after evaporation. However, it is supposed that the basic mechanisms of self-assembled RGO structures by RGO contacts and fluid evaporation within RGO flakes for water or ethanol are same. The porous RGO structures could be formed from interconnected RGO flakes without wrapping surrounded RGO flakes when the water trapped in the RGO precipitates was removed rapidly. The evaporation rates of ethanol at the heated surface were evaluated from the images

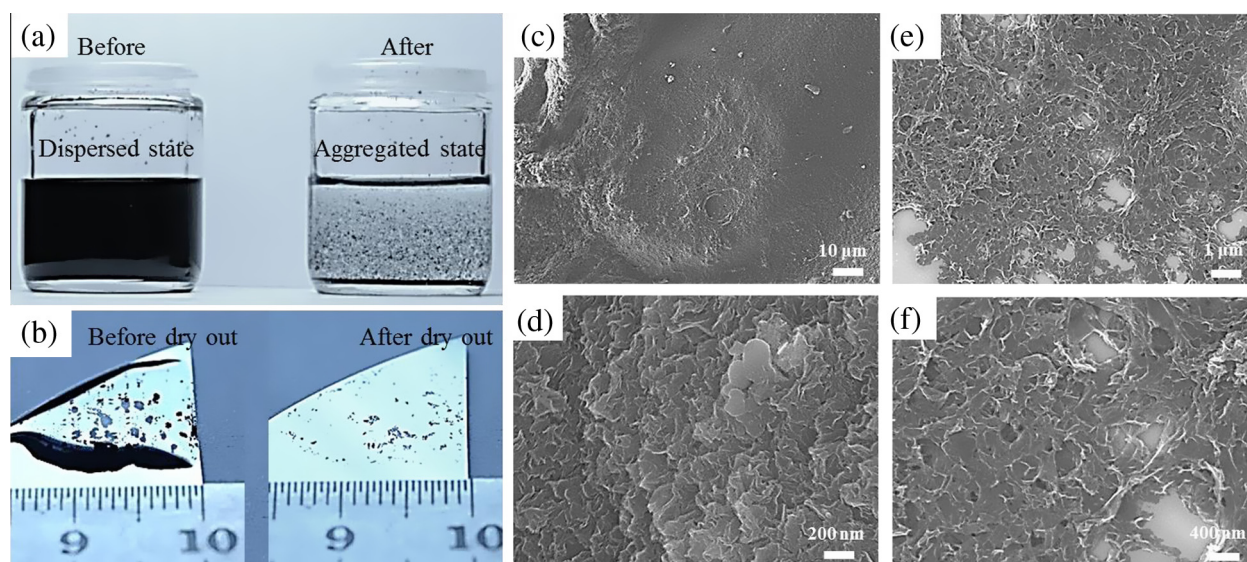


Fig. 6 – (a) 0.3-g/L RGO colloidal dispersion before and after the thermal reaction. Aggregates of RGO following the thermal reaction (b) before and after drying. (c) and (d) SEM images of the shrunken precipitates, with compact structures without pores. (e) and (f) SEM images of the aggregates formed following evaporation of ethanol, which was substituted as the working fluid. (A color version of this figure can be viewed online.)

captured during evaporation. When the surface was heated, the evaporation rate of ethanol was $6.33 \times 10^{-9} \text{ m}^3/\text{s}$, whereas at room temperature, the evaporation rate of ethanol was $7.14 \times 10^{-11} \text{ m}^3/\text{s}$. The evaporation rate of water trapped between RGO sheets during boiling was evaluated from the nucleation images captured using a high-speed camera (Redlake MotionPro Y7). With *heat flux B*, the evaporation rate was $7.53 \times 10^{-6} \text{ m}^3/\text{s}$, which is significantly greater than the evaporation rate of ethanol on the heated surface.

When the concentration of the RGO colloids was low (e.g., 0.05 g/L), precipitates were not produced in the autoclave (see Fig. S5 in the Supplemental materials), and only well-dispersed RGO sheets were observed. At low concentrations, π - π bonds were not induced because of the large distance between RGO sheets and the low rate of making contact between RGO sheets [34,35]. This is consistent with the non-porous structures formed with *heat flux A*. *Heat flux A* did not induce bubble interference, resulting a low rate of making contact between RGO sheets. Consequently, the RGO sheets were not interconnected, similar to the well-dispersed RGO colloids without precipitates that formed at low concentrations. However, the suspended RGO sheets could be deposited on the wrinkled surface during boiling. Such continuous deposition on the surface protrusions resulted in the formation of SBG structures.

With this mechanism, we may expect that control over the size of the pores can be achieved by varying the heat flux. As the heat flux increased, so did the bubble interference, and the boiling was more vigorous, leading to a greater rate of making contact between RGO sheets. This high rate of opportunities for contact induced more complex formations of RGO branches, and the space for water decreased. Furthermore, a larger heat flux induced smaller pores without wrapping due to the faster water evaporation rate. The evaporation dryout mechanism of the RGO complex is not that clear, but it can be the penetrative evaporative front [47]. The pore diameter with a heat flux of $q'' = 18,000 \text{ kW/m}^2$ (*heat flux C*) was in the range 0.22–4.13 μm , and the average pore size was 0.92 μm ; this is significantly smaller than average pore size of 13.11 μm with $q'' = 15,000 \text{ kW/m}^2$. As the heat flux increased to 20,000 kW/m^2 , the pore diameter was in the range 0.19–2.64 μm , and the average pore size was 0.87 μm .

To evaluate the applicability of the SBG and SFG structures, we measured the mechanical strength and electrical conductivity of the self-assembled RGO 3D structures. Structurally, the SBG consisted of wrinkled RGO sheets; however, the SFG was formed of RGO aggregates with some vacancies. Therefore, the SBG had more compact interconnected RGO bonds, and was expected to have greater mechanical strength and better electrical characteristics. The hardness of the SBG was 626.5 MPa, which is approximately 1–2 orders of magnitude greater than that of the SFG structures, which had a hardness in the range 7.76–10.9 MPa. The Young's modulus of the SBG was 14.9 GPa, which is 50 times greater than that of the SFG, and the electrical conductivity of the SBG was 119.7 S/m, which is almost twice that of the SFG.

Although the SBG had better electrical and mechanical properties than the SFG, some applications require 3D porous structures, such as membranes, and biological and chemical reaction areas. Among the porous structures, the SFG that

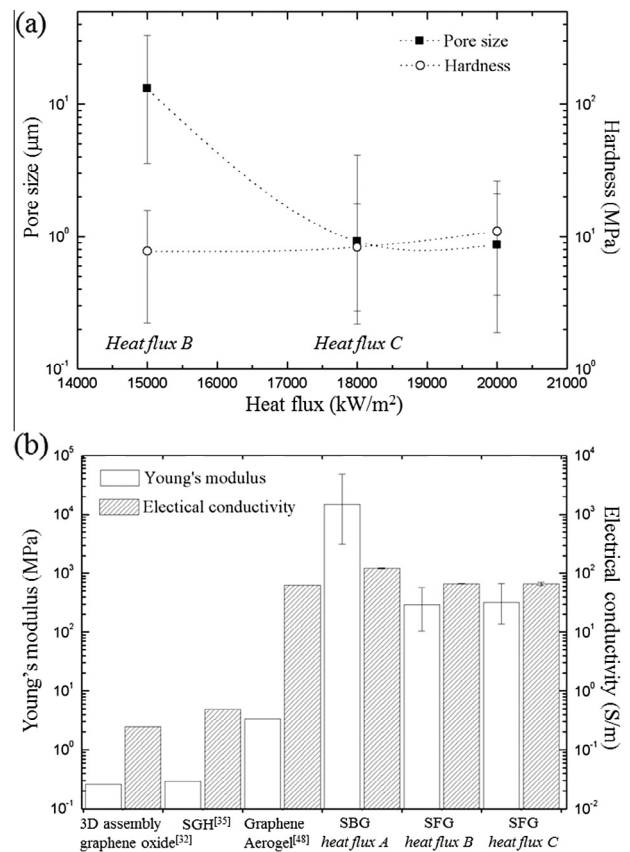


Fig. 7 – (a) Pore and hardness of the SFG as a function of the heat flux. (b) Histogram of the Young's modulus and electrical conductivity showing a comparison of the 3D self-assembled and single-layer graphene oxide promoted using noble metals [32], self-assembled graphene hydrogel (SGH) [35], graphene aerogel [48], SBG, and SFG.

was formed at a high heat flux exhibited better mechanical strength, as shown in Fig. 7a. As the heat flux increased, the Young's modulus of the SFG also increased from 292.5 to 317.9 MPa, which is approximately 100–1000 times greater than the other self-assembled graphene or carbon porous structures, as shown in Fig. 7b. It follows that the interconnected RGO flakes that formed during repetitive expansion and contraction of the triple line during boiling were more strongly bound than those of conventional self-assembled graphene porous structures. Furthermore, the electrical conductivity was 66.5 S/m, which is also larger than that of conventional self-assembled graphene porous structures.

4. Conclusions

We have described the fabricating two types of self-assembled RGO structure – SBG and SFG – by boiling RGO colloidal dispersions. The pore size of these RGO-based structures was controlled by varying the heat flux, and hence the bubble formation rate during boiling. The self-assembled 3D RGO structures exhibited better mechanical and electrical characteristics than the conventional self-assembled graphene or carbon porous 3D structures.

Using this fabrication technique, we can create self-assembled graphene 3D structures with control over the pore size and morphology to promote favorable mechanical and electrical characteristics. Furthermore, the method is low costs, does not require tight control over the environmental conditions, and is rather fast. In addition, the SFG is suitable for large-scale synthesis, and the fabrication is independent of the substrate. Such controllable 3D RGO structures have potential applications in micro-templates for lab-on-a-chip systems, electrocatalysis, supercapacitors, membranes, and biochemical systems.

Acknowledgments

This work was supported by a National Research Foundation of Korea (NRF) grant funded by the Korea government (MSIP) (2012R1A1A2002900).

Appendix A. Supplementary data

Supplementary data associated with this article can be found, in the online version, at <http://dx.doi.org/10.1016/j.carbon.2014.09.068>.

REFERENCES

- [1] Novoselov KS, Geim AK, Morozov S, Jiang D, Zhang Y, Dubonos S, et al. Electric field effect in atomically thin carbon films. *Science* 2004;306(5696):666–9.
- [2] Stankovich S, Dikin DA, Dommett GH, Kohlhaas KM, Zimney EJ, Stach EA. Graphene-based composite materials. *Nature* 2006;442(7100):282–6.
- [3] Geim AK, Novoselov KS. The rise of graphene. *Nat Mater* 2007;6(3):183–91.
- [4] Balandin AA, Ghosh S, Bao W, Calizo I, Teweldebrhan D, Miao F, et al. Superior thermal conductivity of single-layer graphene. *Nano Lett* 2008;8(3):902–7.
- [5] Kuzmenko A, Van Heumen E, Carbone F, Van Der Marel D. Universal optical conductance of graphite. *Phys Rev Lett* 2008;100(11):117401.
- [6] Lee C, Wei X, Kysar JW, Hone J. Measurement of the elastic properties and intrinsic strength of monolayer graphene. *Science* 2008;321(5887):385–8.
- [7] Li X, Wang X, Zhang L, Lee S, Dai H. Chemically derived, ultrasmooth graphene nanoribbon semiconductors. *Science* 2008;319(5867):1229–32.
- [8] Stoller MD, Park S, Zhu Y, An J, Ruoff RS. Graphene-based ultracapacitors. *Nano Lett* 2008;8(10):3498–502.
- [9] Kim KS, Zhao Y, Jang H, Lee SY, Kim JM, Kim KS, et al. Large-scale pattern growth of graphene films for stretchable transparent electrodes. *Nature* 2009;457(7230):706–10.
- [10] Park S, Ruoff RS. Chemical methods for the production of graphenes. *Nat Nanotechnol* 2009;4(4):217–24.
- [11] Maiti UN, Lee WJ, Lee JM, Oh Y, Kim JY, Kim JE, et al. 25th Anniversary article: chemically modified/doped carbon nanotubes & graphene for optimized nanostructures & nanodevices. *Adv Mater* 2014;26(1):40–67.
- [12] Hong W, Xu Y, Lu G, Li C, Shi G. Transparent graphene/pedot-Pss composite films as counter electrodes of dye-sensitized solar cells. *Electrochem Commun* 2008;10(10):1555–8.
- [13] Qu L, Liu Y, Baek J-B, Dai L. Nitrogen-doped graphene as efficient metal-free electrocatalyst for oxygen reduction in fuel cells. *ACS Nano* 2010;4(3):1321–6.
- [14] Wang Y, Shi Z, Huang Y, Ma Y, Wang C, Chen M, et al. Supercapacitor devices based on graphene materials. *J Phys Chem C* 2009;113(30):13103–7.
- [15] Wu Q, Xu Y, Yao Z, Liu A, Shi G. Supercapacitors based on flexible graphene/polyaniline nanofiber composite films. *ACS Nano* 2010;4(4):1963–70.
- [16] Luo Z, Lu Y, Somers LA, Johnson AC. High yield preparation of macroscopic graphene oxide membranes. *J Am Chem Soc* 2009;131(3):898–9.
- [17] Cote LJ, Kim F, Huang J. Langmuir–Blodgett assembly of graphite oxide single layers. *J Am Chem Soc* 2008;131(3):1043–9.
- [18] Eda G, Fanchini G, Chhowalla M. Large-area ultrathin films of reduced graphene oxide as a transparent and flexible electronic material. *Nat Nanotechnol* 2008;3(5):270–4.
- [19] Hernandez Y, Nicolosi V, Lotya M, Blighe FM, Sun Z, De S, et al. High-yield production of graphene by liquid-phase exfoliation of graphite. *Nat Nanotechnol* 2008;3(9):563–8.
- [20] Li X, Zhang G, Bai X, Sun X, Wang X, Wang E, et al. Highly conducting graphene sheets and Langmuir–Blodgett films. *Nat Nanotechnol* 2008;3(9):538–42.
- [21] Wang X, Zhi L, Müllen K. Transparent, conductive graphene electrodes for dye-sensitized solar cells. *Nano Lett* 2008;8(1):323–7.
- [22] Fowler JD, Allen MJ, Tung VC, Yang Y, Kaner RB, Weiller BH. Practical chemical sensors from chemically derived graphene. *ACS Nano* 2009;3(2):301–6.
- [23] Lu CH, Yang HH, Zhu CL, Chen X, Chen GN. A graphene platform for sensing biomolecules. *Angew Chem* 2009;121(26):4879–81.
- [24] Shan C, Yang H, Song J, Han D, Ivaska A, Niu L. Direct electrochemistry of glucose oxidase and biosensing for glucose based on graphene. *Anal Chem* 2009;81(6):2378–82.
- [25] Lee SH, Lee DH, Lee WJ, Kim SO. Tailored assembly of carbon nanotubes and graphene. *Adv Funct Mater* 2011;21(8):1338–54.
- [26] Widawski G, Rawiso M, Francois B. Self-organized honeycomb morphology of star-polymer polystyrene films 1994.
- [27] Lee SH, Kim HW, Hwang JO, Lee WJ, Kwon J, Bielawski CW, et al. Three-dimensional self-assembly of graphene oxide platelets into mechanically flexible macroporous carbon films. *Angew Chem* 2010;122(52):10282–6.
- [28] Yin S, Zhang Y, Kong J, Zou C, Li CM, Lu X, et al. Assembly of graphene sheets into hierarchical structures for high-performance energy storage. *ACS Nano* 2011;5(5):3831–8.
- [29] Vickery JL, Patil AJ, Mann S. Fabrication of graphene-polymer nanocomposites with higher-order three-dimensional architectures. *Adv Mater* 2009;21(21):2180–4.
- [30] Choi BG, Yang M, Hwang WH, Choi JW, Huh YS. 3d Macroporous graphene frameworks for supercapacitors with high energy and power densities. *ACS Nano* 2012;6(5):4020–8.
- [31] Zu S-Z, Han B-H. Aqueous dispersion of graphene sheets stabilized by pluronic copolymers: formation of supramolecular hydrogel. *J Phys Chem C* 2009;113(31):13651–7.
- [32] Tang Z, Shen S, Zhuang J, Wang X. Noble-metal-promoted three-dimensional macroassembly of single-layered graphene oxide. *Angew Chem* 2010;122(27):4707–11.
- [33] Liu F, Seo TS. A controllable self-assembly method for large-scale synthesis of graphene sponges and free-standing graphene films. *Adv Funct Mater* 2010;20(12):1930–6.
- [34] Zhou Y, Bao Q, Tang LAL, Zhong Y, Loh KP. Hydrothermal dehydration for the “green” reduction of exfoliated graphene oxide to graphene and demonstration of tunable optical limiting properties. *Chem Mater* 2009;21(13):2950–6.
- [35] Xu Y, Sheng K, Li C, Shi G. Self-assembled graphene hydrogel via a one-step hydrothermal process. *ACS Nano* 2010;4(7):4324–30.

- [36] Sheng K-X, Xu Y-X, Li C, Shi G-Q. High-performance self-assembled graphene hydrogels prepared by chemical reduction of graphene oxide. *New Carbon Mater* 2011;26(1):9–15.
- [37] Chen Z, Ren W, Gao L, Liu B, Pei S, Cheng H-M. Three-dimensional flexible and conductive interconnected graphene networks grown by chemical vapour deposition. *Nat Mater* 2011;10(6):424–8.
- [38] Maiti UN, Lim J, Lee KE, Lee WJ, Kim SO. Three-dimensional shape engineered, interfacial gelation of reduced graphene oxide for high rate, large capacity supercapacitors. *Adv Mater* 2014;26(4):615–9.
- [39] Shim J, Yun JM, Yun T, Kim P, Lee KE, Lee WJ, et al. Two-minute assembly of pristine large-area graphene based films. *Nano Lett* 2014;14(3):1388–93.
- [40] Ahn HS, Jang J-W, Seol M, Kim JM, Yun D-J, Park C, et al. Self-assembled foam-like graphene networks formed through nucleate boiling. *Sci. Rep.* 2013;3.
- [41] Ahn HS, Kim H, Kim JM, Park SC, Kim JM, Kim J, et al. Controllable pore size of three dimensional self-assembled foam-like graphene and its wettability. *Carbon* 2013.
- [42] Hummers Jr WS, Offeman RE. Preparation of graphitic oxide. *J Am Chem Soc* 1958;80(6):1339.
- [43] Kovtyukhova NI, Ollivier PJ, Martin BR, Mallouk TE, Chizhik SA, Buzaneva EV, et al. Layer-by-layer assembly of ultrathin composite films from micron-sized graphite oxide sheets and polycations. *Chem Mater* 1999;11(3):771–8.
- [44] Li D, Müller MB, Gilje S, Kaner RB, Wallace GG. Processable aqueous dispersions of graphene nanosheets. *Nat Nanotechnol* 2008;3(2):101–5.
- [45] Cao J, Wang Y, Xiao P, Chen Y, Zhou Y, Ouyang J-H, et al. Hollow graphene spheres self-assembled from graphene oxide sheets by a one-step hydrothermal process. *Carbon* 2013;56:389–91.
- [46] Murugan AV, Muraliganth T, Manthiram A. Rapid, facile microwave-solvothermal synthesis of graphene nanosheets and their polyaniline nanocomposites for energy storage. *Chem Mater* 2009;21(21):5004–6.
- [47] Rogers J, Kaviani M. Funicular and evaporative-front regimes in convective drying of granular beds. *Int J Heat Mass Transf* 1992;35(2):469–80.
- [48] Zhang X, Sui Z, Xu B, Yue S, Luo Y, Zhan W, et al. Mechanically strong and highly conductive graphene aerogel and its use as electrodes for electrochemical power sources. *J Mater Chem* 2011;21(18):6494–7.